LETTERS

Nanoscale magnetic sensing with an individual electronic spin in diamond

J. R. Maze[1], P. L. Stanwix[2], J. S. Hodges[1,3], S. Hong[1], J. M. Taylor[4], P. Cappellaro[1,2], L. Jiang[1], M. V. Gurudev Dutt[5], E. Togan[1], A. S. Zibrov[1], A. Yacoby[1], R. L. Walsworth[1,2] & M. D. Lukin[1]

Detection of weak magnetic fields with nanoscale spatial resolution is an outstanding problem in the biological and physical sciences[1–5]. For example, at a distance of 10 nm, the spin of a single electron produces a magnetic field of about 1 μT, and the corresponding field from a single proton is a few nanoteslas. A sensor able to detect such magnetic fields with nanometre spatial resolution would enable powerful applications, ranging from the detection of magnetic resonance signals from individual electron or nuclear spins in complex biological molecules[5,6] to readout of classical or quantum bits of information encoded in an electron or nuclear spin memory[7]. Here we experimentally demonstrate an approach to such nanoscale magnetic sensing, using coherent manipulation of an individual electronic spin qubit associated with a nitrogen-vacancy impurity in diamond at room temperature[8]. Using an ultra-pure diamond sample, we achieve detection of 3 nT magnetic fields at kilohertz frequencies after 100 s of averaging. In addition, we demonstrate a sensitivity of 0.5 μT Hz$^{-1/2}$ for a diamond nanocrystal with a diameter of 30 nm.

Sensitive solid-state magnetometers typically use phenomena such as superconducting quantum interference in SQUIDs[2,3] or the Hall effect in semiconductors[4]. Intriguing avenues such as magnetic resonance force microscopy are also currently being explored[5,6]. Our approach to magnetic sensing[8] uses the coherent manipulation of a single quantum system, an electronic spin qubit. As illustrated in Fig. 1, the electronic spin of an individual nitrogen-vacancy impurity in diamond can be polarized by optical pumping and measured through state-selective fluorescence. Conventional electron spin resonance (ESR) techniques are used to coherently manipulate its orientation. To achieve magnetic sensing, we monitor the electronic spin precession, which depends on external magnetic fields through the Zeeman effect. This method is directly analogous to precision measurement techniques in atomic and molecular systems[9], which are widely used to implement ultra-stable atomic clocks[10–12] and sensitive magnetometers[13].

The principal challenge for achieving high sensitivity using solid-state spins is their strong coupling to the local environment, which limits the free precession time and thus the magnetometer's sensitivity. Recently, there has been great progress in understanding the local environment of nitrogen-vacancy spin qubits, including ^{13}C nuclear spins[7,14–17] and electronic spin impurities[18–20]. Here we use coherent control over a coupled electron–nuclear system[8,16], similar to techniques used in magnetic resonance, to decouple the magnetometer spin from its environment. As illustrated in Fig. 1d, a spin-echo sequence refocuses the unwanted evolution of the magnetometer spin due to environmental fields fluctuating randomly on timescales much longer than the length of the sequence. However, oscillating external magnetic fields matching the echo period will affect the spin dynamics constructively, allowing sensitive detection of its amplitude.

The ideal preparation, manipulation and detection of an electronic spin would yield a so-called quantum-projection-noise-limited minimum detectable magnetic field[12]

$$\delta B_{\min} \approx \frac{\hbar}{g\mu_B\sqrt{T_2 T}} \quad (1)$$

where T_2 is the electronic spin coherence time, T is the measurement time, μ_B is the Bohr magneton, $\hbar$ is Planck's constant divided by 2π, and $g \approx 2$ is the electronic Landé g-factor. In principle, for typical values of $T_2 \approx 0.1$–1 ms, sensitivity of the order of a few nT Hz$^{-1/2}$ can be achieved with a single nitrogen-vacancy centre. Although this is less sensitive than for state-of-the-art macroscopic magnetometers[1,3], a key feature of our sensor is that it can be localized within a region of about 10 nm, either in direct proximity to a diamond surface or within a nano-sized diamond crystal (Fig. 1a). Sensitive magnetic detection on a nanometre scale can then be performed with such a system under ambient conditions. Supplementary Fig. 1 provides a comparison between magnetic field sensitivity and detector volume for several state-of-the-art magnetometers and the nitrogen-vacancy diamond systems demonstrated here.

To establish the sensitivity limits of a single electronic spin magnetometer, we carried out a series of proof-of-principle experiments involving single nitrogen-vacancy centres in bulk ultra-pure single-crystal diamond and in commercially available diamond nanocrystals. Our experimental methodology is outlined schematically in Fig. 1; further details about our experimental set-up and diamond samples are given in Methods. We first focus on the single-crystal diamond bulk sample. Figure 2a shows a typical spin-echo signal observed from an individual nitrogen-vacancy centre. The periodic modulation of the echo is caused by a bath of spin-1/2 ^{13}C nuclei (1.1% natural abundance), which create an effective precessing magnetic field at the nitrogen-vacancy centre of a few microteslas. In the presence of an applied static magnetic field B_{DC}, the periodic Larmor precession of the nuclear field causes the nitrogen-vacancy spin-echo signal to collapse and revive[16] at half the rate of the Larmor frequency of ^{13}C, $\omega_L = \gamma_{13C} B_{DC}$, where γ_{13C} is the carbon gyromagnetic ratio. Note that substantial spin-echo revivals exist even after a free evolution of 0.6 ms. To detect an external AC magnetic field with the highest sensitivity, we must eliminate the contribution from the ^{13}C nuclear field. To this end, the revival rate of the spin-echo signal is adjusted by varying the strength of B_{DC}, such that the frequency of the echo revival peaks coincides with multiples of the AC field frequency (ν) to be detected.

[1]Department of Physics, Harvard University, Cambridge, Massachusetts 02138, USA. [2]Harvard-Smithsonian Center for Astrophysics, Cambridge, Massachusetts 02138, USA. [3]Department of Nuclear Science and Engineering, Massachusetts Institute of Technology, Cambridge, Massachusetts 02139, USA. [4]Department of Physics, Massachusetts Institute of Technology, Cambridge, Massachusetts 02138, USA. [5]Department of Physics and Astronomy, University of Pittsburgh, Pittsburgh, Pennsylvania 15260, USA.

As shown in Fig. 2b, the observed peak of the spin-echo signal varies periodically as the amplitude of the external AC field (B_{AC}) is increased. This signal variation results from phase accumulated by the nitrogen-vacancy spin due to the external AC magnetic field and the resultant time-varying Zeeman shift during the spin's precession; converting this phase into a spin population difference gives rise to variations in the detected fluorescence, which serves as the magnetometer signal. Note that the period of this signal oscillation depends on the spin-echo interval, $\tau = 1/\nu$. For a given value of B_{AC}, the phase accumulated by the electronic spin over one period will increase as the frequency of the external AC field decreases. At the conclusion of a single run of the magnetometry pulse sequence, the measurable spin-echo signal S_B is proportional to the probability of the nitrogen-vacancy spin being in the $m_s = 0$ state: $S_B \propto P_0(B_{AC}) = [1 + F(\tau)\cos(\delta\phi)]/2$, where $\delta\phi = 4g\mu_B B_{AC}/2\pi\nu$ and $F(\tau)$ is the amplitude of the spin-echo signal envelope in the absence of the external AC magnetic field (Fig. 2a).

The sensitivity of the nitrogen-vacancy magnetometer to small variations in B_{AC}, as depicted in the measurements shown in Fig. 2b, is given by $\delta B_{min} = \sigma_S^N / dS_B$, where σ_S^N is the standard deviation of the spin-echo measurement after N averages and dS_B is the slope of the spin-echo signal variation with B_{AC}. Since maximum sensitivity (that is, smallest δB_{min}) occurs at maximum slope, all magnetometer sensitivity measurements were conducted at this point. This maximum slope is proportional to the spin-echo amplitude divided by the frequency of the oscillating field, $dS_B \propto F(1/\nu)/\nu$. For a shot-noise-limited signal with uncertainty σ_S in a single measurement, $\sigma_S^N = \sigma_S/\sqrt{N}$, where $N = T/\tau$. Hence the magnetometer sensitivity is expected to scale as $\delta B_{min} \propto \sqrt{\nu}/F(1/\nu)$.

Figure 3a shows example measurements of the sensitivity δB_{min} after 1 s of averaging as a function of the AC magnetic field frequency, $\nu = 1/\tau$. As this frequency decreases, the accumulated Zeeman phase

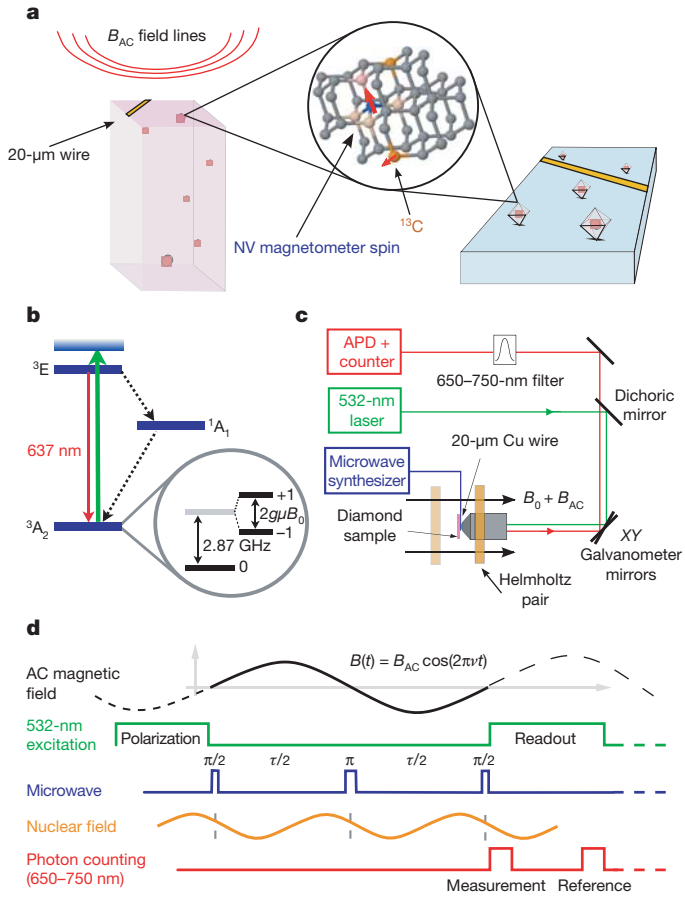

Figure 1 | Principles of the magnetic sensor, which is based on individual nitrogen-vacancy electronic spins in diamond. **a**, A single nitrogen-vacancy impurity (NV) proximal to the surface of an ultra-pure bulk single-crystal diamond sample (left) or localized within a diamond nanocrystal (right) is used to sense an externally applied AC magnetic field (B_{AC}, top left). A 20-μm-diameter wire (yellow) generates microwave pulses to manipulate the electronic spin states. **b**, Level structure of the nitrogen-vacancy centre; see Methods for details. **c**, Diagram of the experimental approach. Single nitrogen-vacancy centres are imaged and localized with ~170 nm resolution using confocal microscopy. The position of the focal point is moved near the sample surface, using a galvanometer mounted mirror to change the beam path and a piezo-driven objective mount. A pair of Helmholtz coils is used to provide both AC and DC magnetic fields. Experiments are then performed on single nitrogen-vacancy centres, as verified by photon correlation measurements. **d**, Optical and microwave spin-echo pulse sequence used for sensing an AC magnetic field, $B_{AC}(\tau)$. An individual centre is first polarized into the $m_s = 0$ sublevel. A coherent superposition between the states $m_s = 0$ and $m_s = 1$ is created by applying a microwave π/2 pulse tuned to this transition. The system freely evolves for a period of time τ/2, followed by a π refocusing pulse. After a second τ/2 evolution period, the electronic spin state is projected onto the $m_s = 0,1$ basis by a final π/2 pulse, at which point the ground state population is detected optically via spin-dependent fluorescence. The DC magnetic field is adjusted to eliminate the contribution of the randomly phased field produced by ^{13}C nuclear spins (gold curve) by choosing $\tau = 2n/\omega_L$, for integer n.

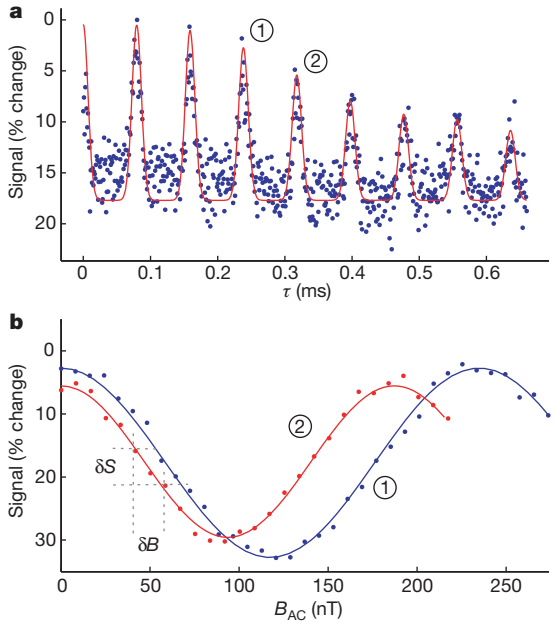

Figure 2 | Demonstration of spin-echo-based magnetometry with an individual nitrogen-vacancy electronic spin in a bulk diamond sample. **a**, Example of electronic spin-echo measurement. We plot the normalized echo signal corresponding to a fractional change of nitrogen-vacancy centre fluorescence. Maximal signal corresponds to an average number of photons $\langle n \rangle = 0.03$ detected during the 324-ns photon counting window of a single experimental run. Collapses and revivals are due to interactions with a ^{13}C nuclear spin bath. The revivals occur at half the rate of the Larmor frequency of ^{13}C (here set by $B_{DC} = 22$ G). The spin-echo signal envelope was fitted with an exponential decay function modulated by a strongly interacting pair of nearby ^{13}C (see Methods). Magnetometer sensitivity experiments are performed at spin-echo revival peaks to maximize signal. Revivals 1 and 2, treated in **b**, are indicated. **b**, Examples of measured spin-echo signal as a function of B_{AC} for two operating frequencies, $\nu_1 = 3.15$ kHz (red) and $\nu_2 = 4.21$ kHz (blue), corresponding to revivals 1 and 2 indicated in **a**. Each displayed point is a result of $N = 7 \times 10^5$ averages of spin-echo sequences. The magnetometer is most sensitive to variations in the AC magnetic field amplitude (δB) at the point of maximum slope, with the sensitivity being limited by the uncertainty in the spin-echo signal measurement (δS). We note that the cosine behaviour of the signal with respect to AC magnetic field amplitude can be changed to a sine by adjusting the phase of the third microwave pulse by 90°. This change moves the point of maximum magnetometer sensitivity to near zero AC field amplitude.

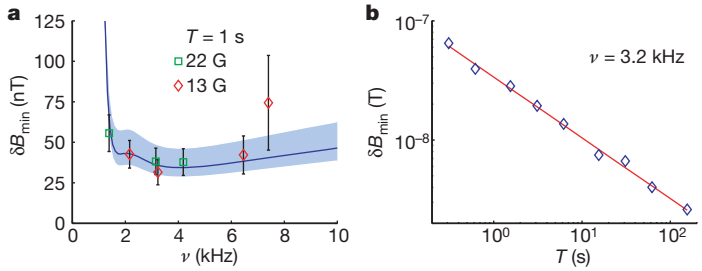

Figure 3 | Characterization of magnetometer sensitivity and minimum measurable AC magnetic field. a, Measured sensitivity of a single nitrogen-vacancy spin magnetometer in a bulk diamond sample over a range of frequencies for the external AC magnetic field after averaging for one second ($T = 1$ s). Error bars, standard deviation (s.d.) for a sample size of 30. Also shown is the theoretically predicted sensitivity (solid blue line), with the shaded region representing uncertainty due to variations in photon collection efficiency (see Methods). Measurements were carried out at two different DC fields, $B_{DC} = 13$ G (in red) and 22 G (in green). **b**, The minimum measurable AC magnetic field as a function of averaging time, for AC field frequency $\nu = 3.2$ kHz and $B_{DC} = 13$ G. Fit to this data (red curve) shows that the sensitivity improves as the square root of the averaging time, and is consistent with theoretical estimates based on photon-shot-noise limited detection.

shift of the nitrogen-vacancy spin during one period increases. This makes the nitrogen-vacancy spin more sensitive to variations of B_{AC} as the frequency is reduced, until the point at which the nitrogen-vacancy spin decoheres during a single period of the external AC magnetic field's oscillation. This decoherence decreases the magnetometer's sensitivity by decreasing the contrast of the spin-echo signal ($F(1/\nu) \rightarrow 0$) and therefore the slope dS_B. At high frequencies or short times, $F(1/\nu) \rightarrow 1$, and the sensitivity scales as $\sqrt{\nu}$. Hence, the magnetometer sensitivity is optimized for frequencies comparable with the longest time for which substantial echo signal is still observable. We note that it is possible to measure at higher frequencies without further loss of sensitivity by using multiple spin-echo pulses in a given measurement period[8]. Figure 3b shows examples of measured nitrogen-vacancy magnetometer sensitivity for a fixed ν as a function of T. The solid line is a fit to $\delta B_{min} \propto T^{-\alpha}$, where $\alpha = 0.5 \pm 0.01$, indicating that magnetic fields as small as few nanoteslas are resolvable after 100 s of averaging.

As noted above, a key feature of our technique is that at specific times, determined by echo revivals, the nitrogen-vacancy electronic spin can be essentially decoupled from ^{13}C nuclear spins. In practice, the decoupling is not perfect, owing to internal dynamics of the electronic environment other than simple spin precession. In fact, the overall decay of the echo signal shown in Fig. 2a does not follow the simple exponential decay associated with typical ESR on bulk samples. This can be understood by noting that the echo dynamics of a single nitrogen-vacancy centre near its revivals is probably determined by a few nearby ^{13}C atoms, which interact strongly with the electronic spin[7,14–16,21], yielding multiple characteristic timescales for echo decay (see Methods).

The absolute sensitivity of the nitrogen-vacancy magnetometer depends on the signal-to-noise ratio in the readout of the nitrogen-vacancy electronic spin state. In the present demonstration, this is limited by photon collection efficiency, which is ~0.1%. The resulting photon shot noise[1,8] is about an order of magnitude larger than the ideal quantum projection noise limit given by equation (1), resulting in a corresponding degradation of magnetometer sensitivity. Our theoretical prediction of magnetometer sensitivity (solid curve in Fig. 3a) combines the nitrogen-vacancy coherence properties shown in Fig. 2a with the noise due to photon counting statistics and imperfect collection efficiency (see Methods). This prediction is in excellent agreement with our experimental results, indicating that our magnetometer is photon-shot-noise limited.

To demonstrate magnetic sensing within a nanoscale detection volume, we also performed similar experiments with single nitrogen-vacancy centres in diamond nanocrystals. We used commercially available nanocrystals that contain a large number of impurities, which shorten the electronic spin coherence time[22] to values ranging from 4 to 10 μs. Sensitive detection of AC magnetic fields is still possible, as demonstrated experimentally in Fig. 4. Here, the echo signal from a single nitrogen-vacancy centre in a 30-nm-size nanocrystal decays on a timescale of ~4 μs. The absence of characteristic collapses and revivals, associated with couplings to ^{13}C nuclear spins, indicates that the echo decay is probably due to other spin impurities, such as paramagnetic substitutional nitrogen atoms containing unpaired electron spins. Magnetic sensing with such a nanocrystal at $\nu = 380$ kHz is demonstrated in Fig. 4b. From these measurements, we estimate a magnetometer sensitivity of $\delta B_{min} \approx 0.5 \pm 0.1\ \mu T\ Hz^{-1/2}$ for this nanocrystal.

Improved magnetometer sensitivity for bulk and nanocrystal diamond may be achieved in several ways. By using isotopically pure diamond with low concentrations of both ^{13}C and nitrogen electron spin impurities, much longer coherence and interrogation times should be possible. For diamond nanocrystals, however, the ultimate sensitivity will eventually be limited by surface effects[19,23]. Increases to the signal-to-noise ratio may also be possible by improving the measurement readout efficiency. Near single-shot readout of an electronic spin in diamond has been achieved with cryogenic cooling using resonant excitation[24]. Photon collection efficiency at room temperature can also be substantially improved using either conventional far-field optics or evanescent, near-field coupling to optical waveguides[25]. Finally, further improvements can probably be obtained by using magnetic sensing with multiple nitrogen-vacancy centres and by using more complex pulse sequences[8].

Our results demonstrate that electronic spins in diamond can be used for precision measurements of nanoscale magnetic fields. This approach opens a new regime of magnetic sensing, enabling detection of single-electron and even nuclear spins separated from

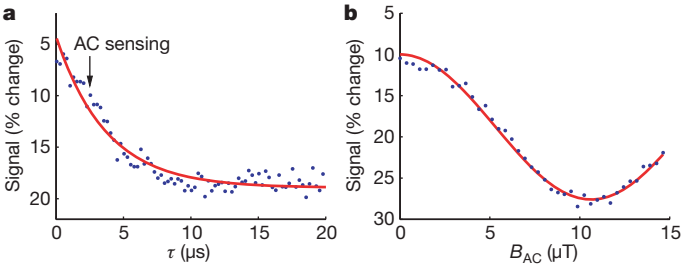

Figure 4 | Demonstration of magnetic sensing with a single nitrogen-vacancy electronic spin in a diamond nanocrystal. a, Example of electronic spin-echo signal from a single nitrogen-vacancy centre contained in a diamond nanocrystal with diameter of 34 ± 12 nm as determined by atomic force microscopy. Maximum signal corresponds to an average number of photons $\langle n \rangle = 0.02$ counted during a 324-ns photon counting window. The arrow indicates the time at which magnetic sensing is performed in **b**. **b**, Example of electronic spin-echo signal as a function of B_{AC} at a frequency of $\nu = 380$ kHz. For these data, $N = 2 \times 10^6$ averages of spin-echo sequences were used. The resulting standard deviation yields a magnetometer sensitivity of $0.5 \pm 0.1\ \mu T\ Hz^{-1/2}$.

nitrogen-vacancy centres by a few tens of nanometres (see Supplementary Information for details). For example, by combining our spin-echo based method with the recently demonstrated[26] transport and manipulation of nanocrystals using an atomic force microscope, a new kind of nanoscale scanning magnetic sensor may be created. Such a sensor could have a wide range of applications, ranging from biological and materials science to quantum information processing and fundamental tests of quantum mechanics. With the aid of field gradients, used for example in approaches based on magnetic resonance force microscopy[5,6], nitrogen-vacancy diamond magnetometers may allow sensing and resolving of individual nuclear spins, with applications in structural biology[8,27]. Our sensing technique also provides an efficient method for measuring single electronic spins in various quantum computing architectures. Furthermore, this technique may allow non-destructive mapping of quantum states into nitrogen-vacancy centres, operating as a quantum magnetic 'head'[28], with possibilities for mechanical transport of quantum information. Finally, we note that our technique could be used for detecting the quantum motion of magnetic mechanical resonators[29,30], with new possibilities for creating non-classical states of mechanical motion and for testing quantum mechanics on a macroscopic scale.

METHODS SUMMARY

AC magnetometry was performed at room temperature on nitrogen-vacancy centres found in both a bulk single-crystal diamond sample and in synthetic diamond nanocrystals (30 nm mean diameter). Single nitrogen-vacancy centres were isolated and probed by confocal microscopy. Phonon-mediated fluorescent emission (630–750 nm) was detected under coherent optical excitation ($\lambda = 532$ nm) using a single photon counting module (APD). As single spots in the confocal image may constitute many nitrogen-vacancy centres, single centres were identified by observing photon antibunching in the measurement of the second-order correlation function.

Green excitation of a nitrogen-vacancy centre also polarized the electronic spin by optical pumping to the $m_s = 0$ sublevel of the $^3A_2$ ground state. The mechanism responsible for optical pumping also provided a means for spin-sensitive detection, as the rate of fluorescence differs for the $m_s = 0$ and $m_s = \pm 1$ states. Coherent manipulation of the spin states was achieved by applying microwave radiation resonant with the $|0\rangle \rightarrow |1\rangle$ transition through a 20 μm wire. A pair of Helmholtz coils provided a static magnetic field to split the degenerate $|\pm 1\rangle$ levels; these coils also produced the external AC magnetic fields sensed with the nitrogen-vacancy magnetometer.

In performing magnetometry, pulsed laser and microwave excitations were defined with an acousto-optic modulator and microwave switch, respectively. As described in Fig. 1d, magnetometer measurements were made for an external AC magnetic field with amplitude B_{AC} and frequency ν, properly phased with respect to the microwave pulses. When the length of the spin-echo sequence (τ) equalled $1/\nu$, the accumulated phase of the electronic spin was proportional to B_{AC}. The fluorescence rate was directly related to this phase. A counting window of 324 ns provided optimal contrast of the fluorescent readout. Many spin-echo cycles were typically averaged to reduce the uncertainty of the photon statistics associated with the low count rate (<1 photon per readout). This technique was sensitive to the projection of the AC magnetic field onto the quantization axis of the electronic spin, corresponding to a vector magnetometer.

Full Methods and any associated references are available in the online version of the paper at www.nature.com/nature.

Received 23 April; accepted 18 July 2008.

1. Budker, D. & Romalis, M. Optical magnetometry. *Nature Phys.* **3,** 227–234 (2007).
2. Bending, S. J. Local magnetic probes of superconductors. *Adv. Phys.* **48,** 449–535 (1999).
3. Kleiner, R., Koelle, D., Ludwig, F. & Clarke, J. Superconducting quantum interference devices: State of the art and applications. *Proc. IEEE* **92,** 1534–1548 (2004).
4. Owston, C. N. A Hall effect magnetometer for small magnetic fields. *J. Sci. Instrum.* **44,** 798–800 (1967).
5. Rugar, D., Budakian, R., Mamin, H. J. & Chui, B. W. Single spin detection by magnetic resonance force microscopy. *Nature* **430,** 329–332 (2004).
6. Mamin, H. J., Poggio, M., Degen, C. L. & Rugar, D. Nuclear magnetic resonance imaging with 90-nm resolution. *Nature Nanotechnol.* **2,** 301–306 (2007).
7. Dutt, M. V. G. *et al.* Quantum register based on individual electronic and nuclear spin qubits in diamond. *Science* **316,** 1312–1316 (2007).
8. Taylor, J. *et al.* High-sensitivity diamond magnetometer with nanoscale resolution. *Nature Phys.* (in the press); preprint at ⟨http://arXiv.org/abs/0805.1367v1⟩ (2008).
9. Budker, D. F., Kimball, D. F. & DeMille, D. P. *Atomic Physics: An Exploration Through Problems and Solutions* (Oxford Univ. Press, 2004).
10. Ludlow, A. D. *et al.* Sr lattice clock at 1×10^{-16} fractional uncertainty by remote optical evaluation with a Ca clock. *Science* **319,** 1805–1808 (2008).
11. Rosenband, T. *et al.* Frequency ratio of Al^+ and Hg^+ single-ion optical clocks; metrology at the 17th decimal place. *Science* **319,** 1808–1812 (2008).
12. Wineland, D. J., Bollinger, J. J., Itano, W. M., Moore, F. L. & Heinzen, D. J. Spin squeezing and reduced quantum noise in spectroscopy. *Phys. Rev. A* **46,** R6797 (1992).
13. Kominis, I. K., Kornack, T. W., Allred, J. C. & Romalis, M. V. A subfemtotesla multichannel atomic magnetometer. *Nature* **422,** 596–599 (2003).
14. Jelezko, F., Gaebel, T., Popa, I., Gruber, A. & Wrachtrup, J. Observation of coherent oscillations in a single electron spin. *Phys. Rev. Lett.* **92,** 076401 (2004).
15. Jelezko, F. *et al.* Observation of coherent oscillation of a single nuclear spin and realization of a two-qubit conditional quantum gate. *Phys. Rev. Lett.* **93,** 130501 (2004).
16. Childress, L. *et al.* Coherent dynamics of coupled electron and nuclear spin qubits in diamond. *Science* **314,** 281–285 (2006).
17. Jiang, L. *et al.* Coherence of an optically illuminated single nuclear spin qubit. *Phys. Rev. Lett.* **100,** 073001 (2008).
18. Hanson, R., Mendoza, F. M., Epstein, R. J. & Awschalom, D. D. Polarization and readout of coupled single spins in diamond. *Phys. Rev. Lett.* **97,** 087601 (2006).
19. Gaebel, T. *et al.* Room-temperature coherent coupling of single spins in diamond. *Nature Phys.* **2,** 408–413 (2006).
20. Hanson, R., Dobrovitski, V. V., Feiguin, A. E., Gywat, O. & Awschalom, D. D. Coherent dynamics of a single spin interacting with an adjustable spin bath. *Science* **320,** 352–355 (2008).
21. Maze, J. R., Taylor, J. M. & Lukin, M. D. Electron spin decoherence of single nitrogen-vacancy defects in diamond. Preprint at ⟨http://arXiv.org/abs/0805.0327⟩ (2008).
22. Rabeau, J. R. *et al.* Single nitrogen vacancy centers in chemical vapor deposited diamond nanocrystals. *Nano Lett.* **7,** 3433–3437 (2007).
23. Rabeau, J. R. *et al.* Implantation of labelled single nitrogen vacancy centers in diamond using ^{15}N. *Appl. Phys. Lett.* **88,** 023113 (2006).
24. Wrachtrup, J. & Jelezko, F. Processing quantum information in diamond. *J. Phys. Condens. Matter* **18,** S807–S824 (2006).
25. Chang, D. E., Sorensen, A. S., Hemmer, P. R. & Lukin, M. D. Quantum optics with surface plasmons. *Phys. Rev. Lett.* **97,** 053002 (2006).
26. Balasubramanian, G. *et al.* Nanoscale imaging magnetometry with diamond spins under ambient conditions. *Nature* doi:10.1038/nature07278 (this issue).
27. Degen, C. L. Scanning magnetic field microscope with a diamond single-spin sensor. Preprint at ⟨http://arXiv.org/abs/0805.1215v2⟩ (2008).
28. Cirac, J. I. & Zoller, P. A scalable quantum computer with ions in an array of microtraps. *Nature* **404,** 579–581 (2000).
29. Treutlein, P., Hunger, D., Camerer, S., Hansch, T. W. & Reichel, J. Bose-Einstein condensate coupled to a nanomechanical resonator on an atom chip. *Phys. Rev. Lett.* **99,** 140403 (2007).
30. Rabl, P. *et al.* Strong magnetic coupling between an electronic spin qubit and a mechanical resonator. Preprint at ⟨http://arXiv.org/abs/0806.3606⟩ (2008).

Supplementary Information is linked to the online version of the paper at www.nature.com/nature.

Acknowledgements We acknowledge A. Akimov, D. Budker, F. Jelezko, F. Koppens, A. Trifonov, P. Hemmer and J. Wratchtrup for many discussions and experimental assistance. This work was supported by the NSF, DARPA, the Packard Foundation and Harvard CNS.

Author Information Reprints and permissions information is available at www.nature.com/reprints. Correspondence and requests for materials should be addressed to M.D.L. (lukin@fas.harvard.edu).

METHODS

Samples. AC magnetometry was performed at room temperature on nitrogen-vacancy centres in both a bulk single-crystal diamond sample (1 mm × 1 mm × 0.5 mm, natural diamond with an atypically low nitrogen concentration) and in diamond nanocrystals (monocrystalline, synthetic diamonds, 30 nm mean diameter, purchased from Microdiamant) deposited on a quartz coverslip.

Confocal set-up. Single nitrogen-vacancy centres were isolated and probed via confocal microscopy. Phonon-mediated fluorescent emission (630–750 nm) was detected under coherent optical excitation ($\lambda = 532$ nm) using a single photon counting module (Perkin-Elmer SPCM-AQRH-13). The density of nitrogen-vacancy centres in both the bulk single-crystal and nanocrystal samples were sufficiently low that single bright spots (within the approximate confocal volume of 200 nm × 200 nm × 500 nm) were resolvable from the background fluorescence. As single spots in the confocal image may constitute many nitrogen-vacancy centres, single centres were identified by observing photon antibunching in the measurement of the second-order correlation function. This emission was separated from the excitation path using a dichroic mirror, and also notch and longpass filters. Samples were imaged with an oil immersion objective lens (Nikon CFI Plan Fluor Series, NA = 1.3, 100× magnification) over a 50 μm × 50 μm area in the plane normal to the optical path. Two galvanometer controlled mirrors steered the beam path for rapid imaging of this area. Experimental drifting of the focal plane due to thermal effects was compensated by using closed-loop feedback of the galvanometer and objective piezo voltages.

Single-centre electron spin resonance. The nitrogen-vacancy centre $^3A_2$ ground state consists of two unpaired electrons in a triplet configuration leading to a zero-field splitting ($\Delta = 2.87$ GHz) between the $m_s = 0$ and $m_s = \pm 1$ sublevels. Coherent optical excitation at $\lambda = 532$ nm optically pumped the ground state into its $m_s = 0$ sublevel. In addition, an external static magnetic field produced by a pair of Helmholtz coils split the degeneracy between the $m_s = \pm 1$ states. It was then possible to selectively address transitions between the $m_s = 0$ and $m_s = 1$ (or $m_s = -1$) states with microwave radiation (Fig. 1b) and manipulate a two-level subspace of the spin triplet (for example with spin-echo pulse sequences). Microwave radiation was applied by using the magnetic field emanating from a 20 μm wire placed on the surface of the samples.

The excited (^3E) state decay rates, also responsible for optical pumping, provided a means for spin-sensitive detection, as the rate of fluorescence was reduced for the $m_s = \pm 1$ states compared to the $m_s = 0$ states, with >35% contrast. The spin state in the ground electronic state was measured by pulsing on green excitation and monitoring the total number of photons collected within the optimal measurement interval, 324 ns. A 300 MHz PulseBlaster ESR pulse generator was employed for timing the triggering of counters, microwave pulses, the AC magnetic field, and the excitation laser. Microwave pulses were provided by gating the output of a frequency synthesizer with a microwave switch, while green laser pulses were generated using an acousto-optic modulator. The π and π/2 pulses used for the spin-echo sequence were calibrated from the Rabi nutation curves between the two spin states.

AC magnetometry. As described in Fig. 1d and in ref. 8, demonstration magnetometer measurements were performed for an externally applied AC magnetic field with amplitude B_{AC}, frequency ν, and phase ϕ_{AC} during a cycle of a spin-echo sequence with a period τ. The accumulated phase of the spin superposition state

$$\delta\phi = \frac{4g\mu_B B_{AC}}{2\pi\nu}\sin^2\left(\frac{\pi\nu\tau}{2}\right)\cos(\pi\nu\tau + \phi_{AC}) \quad (2)$$

contained information about the projection of the AC magnetic field amplitude onto the quantization axis of the electronic spin, corresponding to a vector magnetometer. Oscillatory magnetic fields from 1–10 kHz were generated by modulating the current through a Helmholtz pair also used to apply a bias DC magnetic field. For application of higher frequency AC fields (100–300 kHz), a single coil (60 turns) was resonantly driven and placed near the sample.

The measured signal intensity S_B was a function of the accumulated phase $\delta\phi$, as given by the probability of being in the $m_s = 0$ state after the spin-echo pulse sequence: $S_B \propto P_0(B_{AC}) = [1 + F(\tau)\cos(\delta\phi)]/2$. Ideally, for a single-shot measurement of B_{AC} the sensitivity was maximized for a particular ν by setting $\tau = 1/\nu$. In practice, many spin-echo cycles were averaged to reduce the uncertainty in photon statistics given the low single-shot count rate. To this end, the period of the entire measurement sequence (including polarization and readout, Fig. 1d) was matched to $1/\nu$ in order to avoid multiple offset phases ϕ_{AC} when the periods were incommensurate. The dependence on ϕ_{AC} was removed entirely by appropriately shifting the time origin of the measurement pulse train. As the polarization ($\tau_p = 1$ μs) and readout ($\tau_r = 3$ μs) periods were short compared to the oscillation periods for typical 1–10 kHz AC magnetic fields, this choice introduced a slight deviation ε from the optimal $\delta\phi$, as $\tau_p + \tau_r + \tau = 1/\nu \rightarrow \tau\nu = 1 - \varepsilon$. The overall sensitivity was thus slightly reduced from its optimal value as $1 - \mathcal{O}(\varepsilon^2)$. For all experiments presented here, $\nu\tau = 0.88$ was used. The envelope of the spin-echo signal, $F(\tau)$ (see, for example, Fig. 2a) was modelled with an exponential decay modulated by the effect of a pair of nearby strongly interacting ^{13}C nuclear spins. In this model[21], $F(\tau) = \exp(-(\tau/T_2)^4)(1 - [(a^2 - b^2)/a^2]\sin^2(a\tau)\sin^2(b\tau))$; where for the data in Fig. 2a we found $T_2 = 676$ μs, $b = 478$ Hz (corresponding to the dipolar interaction between the two nuclei) and $a = 626$ Hz (corresponding to the interactions between the nuclei and the nitrogen-vacancy spin). Using these experimentally determined parameters, the above model provided a prediction for the magnetometer sensitivity[8] $\eta_{AC} = \pi\hbar/(g\mu_B C\sqrt{\nu}F(1/\nu))$ as a function of frequency (solid curve in Fig. 3a), where $g \approx 2$ is the electron g-factor, μ_B is the Bohr magneton, and $C^{-2} = 1 + 2(a_0 + a_1 + a_0a_1)/(a_0 - a_1)^2$ is a factor that estimates[8] the photon shot noise when the average photon number during the readout window of 324 ns is much less than 1. The values $a_0 = 0.03 \pm 0.006$ and $a_1 = 0.018 \pm 0.004$ were the average numbers of detected photons for the electronic spin states $m_s = 0$ and $m_s = \pm 1$, respectively.